Marine and Petroleum Geology 162 (2024) 106730

Contents lists available at ScienceDirect

Marine and Petroleum Geology

journal homepage: www.elsevier.com/locate/marpetgeo

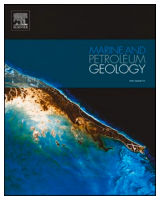

The formation of the Paleocene lacustrine organic-rich shale in the Subei Basin, East China associated with the early late Paleocene event and marine incursions

Ming Guan [c], Xiaoping Liu [a,b,*], Zhijun Jin [d,e,**], Wenzhi Zhao [c], Wei Liu [c], Leibo Bian [c], Jin Dong [c], Xu Zeng [c], Bang Zeng [a,b], Biao Sun [a,b], Hanxi Liu [f], Zibin Wang [g]

[a] National Key Laboratory of Petroleum Resources and Engineering, China University of Petroleum (Beijing), Beijing, China, 102249
[b] College of Geosciences, China University of Petroleum (Beijing), Beijing, 102249, China
[c] Research Institute of Petroleum Exploration and Development, China National Petroleum Corporation, Beijing, 100083, China
[d] Institute of Energy, Peking University, Beijing, 100871, China
[e] State Key Laboratory of Shale Oil and Gas Enrichment Mechanisms and Effective Development, Beijing, 100083, China
[f] Research Institute of Petroleum Exploration Development, PetroChina Xinjiang Oilfield Company, Karamay, Xinjiang, China
[g] No.1 Oil Production Plant, PetroChina Dagang Oilfield Company, Tianjin, China

ARTICLE INFO

Keywords:
Lacustrine shale
Geochemistry
Paleoenvironment
Saline condition
Organic matter accumulation

ABSTRACT

The second member of the Funing Formation (E_1f^2) is a Paleocene lacustrine organic-rich shale and has been identified as a primary source rock for both conventional and unconventional oil and gas in East China. It is correlated with the Early Late Paleocene Event (ELPE), a significant temperature inflection point in the Paleocene. However, the impact of the ELPE on the lacustrine organic-rich sedimentation is still not well understood. This study pinpoints the ELPE in the lacustrine E_1f^2 shale of the Subei Basin, identifies the resultant marine incursions by biomarkers, correlates the ELPE, marine incursions, and the depositional process, and clarifies organic matter accumulation mechanisms in the E_1f^2 shale. The interval preceding the ELPE has relatively low organic matter content, having been deposited in an arid paleoclimate with saline water conditions and low productivity. Eukaryotes predominantly contributed to the organic matter accumulation. The ELPE is identified in the E_1f^2 shale by negative carbonate carbon and oxygen isotope excursions. Subsequently, increasing temperatures and rising global sea levels induced marine incursions into the Subei Basin, supported by the appearance of 24-*n*-propylcholestane and the $C_{30}/C_{27\text{-}30}$ steranes ratio. The interval following the ELPE shows relatively high organic matter content and was deposited in an arid to semihumid-semiarid climate and a saline to brackish waterbody. Marine incursions likely introduced nutrients and enhanced lacustrine productivity, as indicated by the consistency between signals of marine invasion and bioavailable nutrient elements. Different origins contribute to organic matter accumulation at this stage, with prokaryotes being more dominant than eukaryotes. The E_1f^2 shale provides valuable insights into lacustrine organic-rich sedimentary processes and the responses of lacustrine systems to global events.

1. Introduction

Organic-rich sediments are formed through a sequence of deposition and diagenesis processes (Ilgen et al., 2017; Rimstidt et al., 2017). These can provide key insights into paleoenvironments through geological time (Rimmer et al., 2004; Ross and Bustin, 2009). Additionally, the abundant organic matter in shale lays the foundation for hydrocarbon generation. There has been increasing attention concerning organic matter's heterogeneous distribution and subsequent influence on shale oil and gas prospects, which inspires us to understand its accumulating mechanism in shale (Chen et al., 2015; Zou et al., 2019). High primary productivity promotes the formation of abundant planktonic microorganisms that eventually settle on the lake or sea floor (Huc et al., 1986; Kuypers et al., 2002), and favorable depositional and burial water

* Corresponding author. College of Geosciences, China University of Petroleum (Beijing), Beijing 102249, China.
** Corresponding author. Institute of Energy, Peking University, Beijing, 100871, China.
E-mail addresses: liuxiaoping@cup.edu.cn (X. Liu), jinzj57@pku.edu.cn (Z. Jin).

https://doi.org/10.1016/j.marpetgeo.2024.106730
Received 29 November 2023; Received in revised form 22 January 2024; Accepted 23 January 2024
Available online 28 January 2024

conditions (redox, salinity, stratification) enhance the conditions of organic matter accumulation and preservation (Demaison and Moore, 1980; Tyson, 2005). The formation of organic-rich sediments is closely linked to global or local geological events, such as volcanic eruptions, deep hydrothermal fluids, eustatic variations, anoxic events, etc. (Demaison and Moore, 1980; Keller, 2005; Smith and Harper, 2013).

Sea-lake connection events have been well documented in many lacustrine basins, such as the Salt IV Formation of the Mulhouse Basin (Sinninghe Damsté et al., 1993), the Mirador Formation of the Eastern Colombia (Santos et al., 2008), the Haotaoyuan Formation of the Nanxiang Basin (Xia et al., 2019), the Shahejie Formation of the Bohai Bay Basin (Xu et al., 2019), the Lokbatan section of the Plio-Pleistocene in the South Caspian Basin (Hoyle et al., 2021), the Nenjiang Formations of the Songliao Basin (Liu et al., 2022), and the Ganchaigou Formation in the Qaidam Basin (Ma et al., 2022), etc., potentially impacting the hydrology and the formation of organic-rich shale in lacustrine systems. In the Subei Basin, where the second member of the Funing Formation (E_1f^2, 60.2–58 Ma) serves as the primary source rock (Liu et al., 2017; Su et al., 2022), various marine geological and geochemical signals suggest that marine incursions occurred, including the similar glauconite occurrence in the Funing Formation to that in the Yangtze Delta and coastal zone of Jiangsu-Zhejiang Region, *clupeidae* and *tungtingichthys* that are related to marine condition, and seabird fossils (Fu et al., 2007). Marine incursions into lacustrine basins can affect lake water chemistry and circulation patterns, trigger limnological changes, and potentially drive fast and catastrophic turnovers in biodiversity (Santos et al., 2008; Marzocchi et al., 2016; Virtasalo et al., 2016; Song et al., 2021). It has a knock-on effect on ecosystems and depositional processes, which are potentially favorable to organic matter accumulation. Rising sea levels inducing marine incursions into the lacustrine basin may be linked to the Early Late Paleocene Event (ELPE, 58.9 Ma, lasting for approximately 52–53 k.y.), which implies a potential link between EPLE and marine incursions that might have influenced the deposition process of the E_1f^2 shale. The ELPE is a global phenomenon that marked an abrupt climate shift, transitioning from a long-term mid-Paleocene cooling phase to a sustained warming period (Petrizzo, 2005; Bernaola et al., 2007; Hollis et al., 2012). It has been reported in various geological records, including deep sea cores of the North Pacific and South Atlantic (Petrizzo, 2005; Bralower et al., 2006; Westerhold et al., 2008, 2011), marine sections of the western Pyrenees (Bernaola et al., 2007), and lacustrine outcrops in Spain and Argentina (Hyland et al., 2015; Coccioni et al., 2019), etc. Therefore, the E_1f^2 shale offers an excellent case for exploring lacustrine responses to ELPE and the relevant impact of marine incursions on organic matter accumulation.

In this study, vertical variation of organic matter abundance in the E_1f^2 shale was depicted within a high-frequency sequence stratigraphic framework, the intervals affected by marine incursions were identified, and the paleoenvironment during the deposition of the E_1f^2 shale was reconstructed using geochemical proxies. This study aimed to constrain the span of the marine incursion episode, discuss the environmental consequences of marine incursions, and elucidate the organic matter accumulation mechanism in lacustrine shales. The presented case provides evidence of the effects of global events on lacustrine shale systems and has implications for the heterogeneous distribution evaluation in shale oil and gas systems.

2. Geological setting

The Subei Basin is situated in eastern China and covers an area of approximately 38,000 km^2 (Fig. 1a). It has undergone multiple tectonic movements since the Cretaceous, including regional depression in the Late Cretaceous, fault depression in the Paleogene, and overall subsidence in the Neogene, resulting in the structural framework of "two depressions and an uplift" (Fig. 1b) (Shu et al., 2005; Liu et al., 2017). The Paleogene Funing Formation was deposited during the transitional period from depression to rift basin during the Wubao movement (Fig. 2a) (Chen, 2010; Liu et al., 2017). It comprises a mixture of lacustrine sediments, including fluvial, transitional, and lacustrine deposits, which are segmented into four members, ascending from the first to the fourth. The E_1f^2 is represented by fine-grained sediment of semi-deep to deep lake facies, mostly dark limy or dolomitic shale or mudstone (Figs. 2b and 3a-e). Furthermore, carbonate and organoclay laminae are commonly observed in the E_1f^2 shale (Fig. 3a, b and e).

A chronostratigraphic framework of the Subei Basin is established (Fig. 2a) according to lithology, palynology, biostratigraphy, stratigraphic sequence (Zhou et al., 1982; Zhao et al., 1993; Zhang et al., 2004; Shu et al., 2005; Wei et al., 2011), and basaltic K–Ar geochronology (Yang et al., 1998). The E_1f^2 is thought to have been deposited between 60.2 and 58.0 Ma (Zhou et al., 2019; Su et al., 2022). A third-order sequence consists of the second and the third member of the

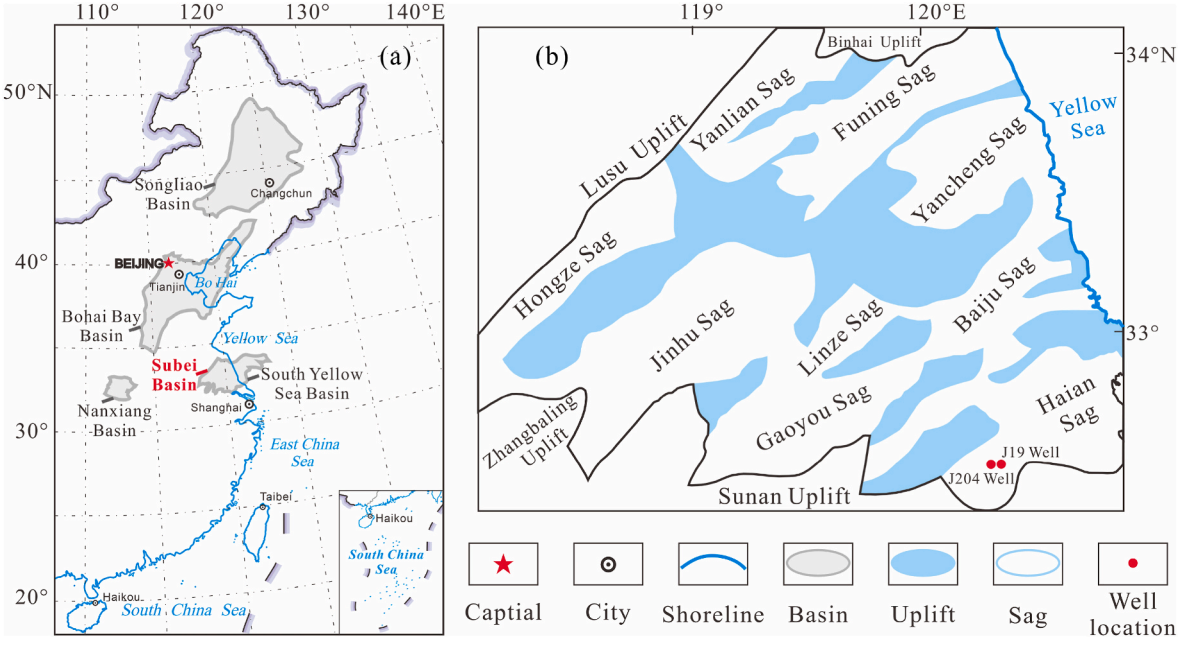

Fig. 1. The location of the Subei Basin (a) (Li et al., 2012) and its structural framework (b) (Chen, 2010).

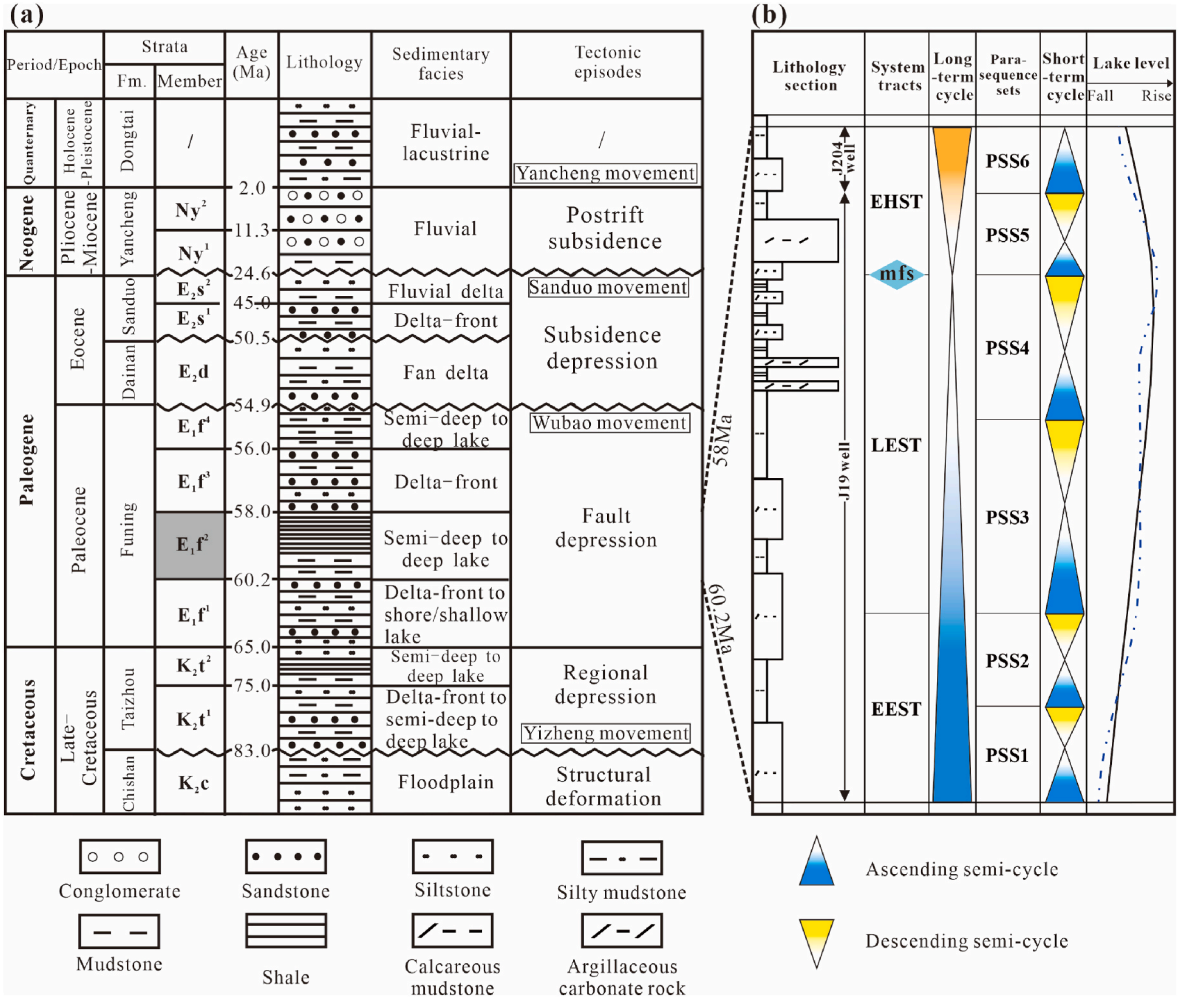

Fig. 2. Lithological column and stratigraphic division from the Late Cretaceous to the Neogene in the Subei Basin (a) (Ran et al., 2012). The lithological column and the sequence stratigraphic framework of the E_1f^2 shale, including three system tracts in third-order sequence and six parasequence sets (b) (Guan et al., 2022). EEST = early expanding system tract; LEST = late expanding system tract; EHST = early highland system tract; mfs = maximum flood surface; PSS = parasequence set.

Funing Formation (Ran et al., 2012). The E_1f^2 has been identified as a part of the third-order sequence and consists of six fourth-order sequences (i.e., parasequence set (PSS)), ascending from PSS1 to PSS6 (Fig. 2b) (Guan et al., 2022). As the predominant source rock of the Subei Basin, the E_1f^2 shale has attracted attention in recent shale oil exploration in terms of shale oil accumulation conditions and resource potential (Liu et al., 2020; Guan et al., 2022).

3. Methods

A total of 110 samples were collected from the J19 and the J204 wells from the deep lake facies, including 94 cores and 16 cuttings. Samples of PSS1-PSS5 are from the J19 well, while the counterparts of PSS6 are from the J204 well. Total organic carbon (TOC) content was determined for all samples. Among them, 23 samples were selected for Rock-Eval, solvent extraction, bitumen fractionation, gas chromatography-mass spectrometry (GC-MS), and isotope analysis at the China University of Petroleum-Beijing; the sample from 3825.05 m was used for gas chromatography-metastable reaction monitoring-gas chromatography-mass spectrometry (MRM-GC-MS) at the China University of Petroleum-Beijing; and 42 samples were selected for elemental analysis at the Beijing Research Institute of Uranium Geology.

3.1. TOC and Rock-Eval

Approximately 100 mg of powdered samples were introduced into a LECO CS-200 Carbon/Sulfur Analyzer to measure TOC after eliminating inorganic carbon by dropwise adding dilute hydrochloric acid (HCl). About 100 mg of powdered shale samples were placed into an OGE-II Analyzer to obtain pyrolysis parameters, including free hydrocarbons (S_1), generatable hydrocarbons (S_2), peak pyrolysis generation temperature (Tmax), and hydrogen index (HI).

3.2. Organic composition analysis

Approximately 30 g of powdered samples were extracted using dichloromethane as the solvent to obtain extractable organic matter (EOM). Asphaltenes were precipitated from EOM using *n*-hexane. Subsequently, the aliphatic, aromatic, and resin fractions were separated by a chromatographic column and different eluents, including *n*-hexane, a 2:1 (v/v) mixture of dichloromethane and *n*-hexane, and a 1:1 (v/v) mixture of ethanol and dichloromethane.

The GC-MS analysis of aliphatic fractions was performed on an Agilent 6890 Gas Chromatograph coupled to an Agilent 5975i Mass Selective Detector. The gas chromatograph was equipped with an HP-5MS elastic silica capillary column (60 m × 0.25 mm i.d., 0.25 μm film thickness) using helium as the carrier gas.

The MRM-GC-MS analysis of the aliphatic fraction was carried out on

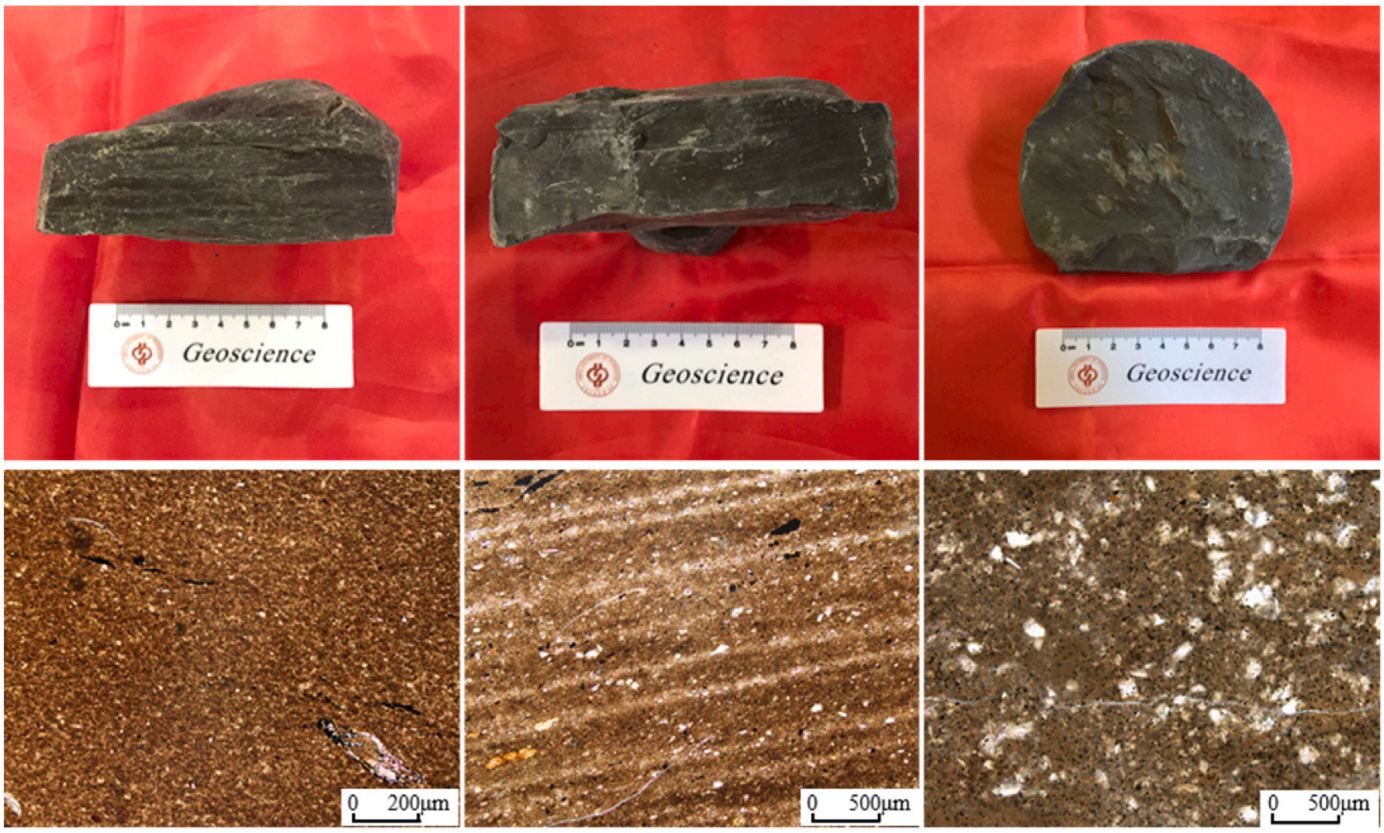

Fig. 3. Hand sample and thin-section images showing that the E_1f^2 shale have high carbonate content and laminated structure: (a) J204 well, 4023.22 m, laminated calcareous shale; (b) J19 well, 3862.58 m, laminated shale; (c) J19 well, 4028.77 m, lime mudstone; (d) J19 well, 3811.51 m, mudstone; (e) J19 well, 3824.6 m, laminated limy shale with many biodebris; and (f) J19 well, 3883 m, dolomitic mudstone.

a Thermo Fisher TSQ8000 Evo MS equipped with an Agilent 6890 Gas Chromatograph and an HP-5MS elastic silica capillary column (60 m × 0.25 mm i.d., 0.25 μm film thickness) using helium as the carrier gas. The following mass-to-charge ratio (m/z) transitions were selected to examine the C_{26}–C_{30} steranes: 358 > 217, 372 > 217, 386 > 217, 400 > 217, 414 > 217, and 414 > 231 (Xu et al., 2019).

3.3. Isotope analysis

Powdered samples were pretreated with hydrogen peroxide to remove organic carbon. The residues were rinsed with distilled water and then dried at 105 °C for 2 h. About 5 mg of samples were reacted with 100 % orthophosphoric acid (H_3PO_4) at 75 °C for at least 2 h, and the evolved CO_2 derived from carbonate minerals in the shale samples was isotopically determined by an Elemental Isoflow-Precision Mass Spectrometer. Carbon and oxygen isotopic values ($\delta^{13}C_{carb}$ and $\delta^{18}O$) are reported in per mil relative to the international Vienna PeeDee Belemnite (VPDB) using IAEA-603 and IAEA–CO–8-Calcite international standards. The uncertainty was 0.2 ‰ for $\delta^{18}O$ values and was ±0.3‰ for $\delta^{13}C$ values.

Samples were combusted at 850 °C after decarbonating using diluted HCl, and the evolved CO_2 from organic matter in the shale samples was analyzed by an Elemental Analyzer-Precision Mass Spectrometer. The organic carbon isotope ($\delta^{13}C_{org}$) values were standardized to the international VPDB using USGS-61 Caffeine, USGS-62 Caffeine, and USGS Caffeine. The uncertainty in $\delta^{13}C_{org}$ values was ±0.5‰.

3.4. Elemental analysis

Powdered samples were heated to 1000 °C in a muffle furnace to determine the percentage of loss on ignition (LOI). Approximately 500 mg of sample was mixed with 4 g of anhydrous lithium tetraborate at 1200 °C to make a fusion glass disk. Major element abundance analyses were then performed on the disk by an AB104L, Axios-Max Wavelength Dispersive X-ray Fluorescence Spectrometer. The analytical precision of trace element abundance was ±5 %. Appropriately 25 mg of sample was mixed with 1 mL hydrofluoric acid (HF) and 0.5 mL of nitric acid (HNO_3) for 24 h at 185 °C. The residues were completely dissolved in 5 mL of HNO_3 for 3 h at 130 °C. The solutions were diluted with distilled water to 25 mL and then used to measure trace element contents using an Element XR Plasma Mass Spectrometer. The analytical precision of trace element abundance was ±5 %. The enrichment factor of a given element (X_{EF}) represents the enrichment or depletion level and can be determined through $(X/Al)_{sample}/(X/Al)_{PAAS}$, where PAAS is Post-Archean Austrialian Shale (Taylor and McLennan, 1985). The chemical weathering index (CIA) is calculated by $[Al_2O_3/(Al_2O_3 + CaO^* + Na_2O + K_2O)] \times 100$ (Nesbitt and Young, 1982). CaO* means the CaO molar content in silicate and can be calculated by $CaO^* = CaO - P_2O_5 \times 10/3$; if the resulting CaO* is more than the Na_2O content, the Na_2O content will be adopted to represent the CaO* value (Mclennan et al., 1993).

4. Results

4.1. Bulk geochemical characteristics

Within the E_1f^2 shale, the PSS5 exhibits the highest TOC content among all PSSs, ranging from 0.79 % to 3.95 % with an average of 2.51 %. This is followed by PSS4, where the mean TOC is approximately 1.31 %. In PSS3 and PSS6, the TOC values are moderate, with averages of 1.17 % and 1.19 %, respectively. At the beginning of the PSSs, the TOC values are slightly lower, with a mean of 0.89 % in the PSS2 and 1.09 %

in the PSS1. However, it is observed that the TOC in all selected samples is mostly above 1 % (Fig. 4, Supplementary Table 1). Organic matter types are identified using the relationship between HI and Tmax. The E_1f^2 shale shows a blend of type II and type III. The intervals of PSS1-PSS3 are dominated by type III and have some samples of type II; PSS4 is mainly type II_2; and the intervals of PSS5-PSS6 are mainly type I and type II (Fig. 5).

4.2. Biomarkers

The ratio of 5α(H), 14β(H), 17β(H) and 5α(H),14α(H),17α(H) 20R ethylsteranes ($C_{29}ββ/(αα+ββ)$) increases from close to zero to an equilibrium value of 0.67–0.71 with increasing thermal maturity and can be used to evaluate thermal maturity (Seifert and Moldowan, 1986). However, it is necessary to integrate other maturity parameters to make an accurate evaluation of thermal maturity because $C_{29}ββ/(αα+ββ)$ values might not reach equilibrium during the peak oil generation in some Tertiary sequences (Grantham, 1986) and bring about an undervaluation of these source rocks' maturity. In this study, this ratio increases from 0.36 to 0.61 downward (Fig. 6b). The ratio of pristane to phytane (Pr/Ph) is related to redox conditions and varies widely from 0.31 to 2.83, with an average of 0.78. The Pr/Ph ratio remains relatively low (<0.3) from PSS1 to mid-PSS4, after which it rapidly increases to above 0.7 from up-PSS4 to PSS6 (Fig. 6c). Gammacerane is closely related to water body stratification that is usually attributed to a saline water or evaporative environment (Sepúlveda et al., 2009). The ratio of gammacerane to C_{30} hopance ($Ga/C_{30}H$) varies from 0.01 to 1.87, with a mean of 0.49. The $Ga/C_{30}H$ values show periodic fluctuation during PSS1 to mid-PSS4, increasing in PSS1 and PSS3 and decreasing in PSS2 and down-PSS4. From up-PSS4 to PSS6, the ratio remains relatively low (<0.2) (Fig. 6d). The ratio of steranes to hopanes is usually used to estimate the relative contribution of eukaryotes to prokaryotes in source rocks (Moldowan et al., 1985). The ratio of $C_{27\text{-}29}$ steranes to $C_{29\text{-}35}$ hopanes (S/H) varies from 0.06 to 1.76, with an average of 0.50. Vertically, the S/H values show a similar pattern to the $Ga/C_{30}H$ ratios (Fig. 6e). The raito of C_{19} to C_{23} tricyclic terpanes (C_{19}/C_{23} TT) is associated with terrigenous organic matter input, keeping low values from PSS1 to down-PSS4 and gradually increasing from up-PSS4 to PSS6 (Fig. 6f) (Supplementary Table 2).

4.3. Elemental geochemistry

The ratio of strontium to cupper (Sr/Cu) reflects paleoclimate (Xu et al., 2021). There are relatively low Sr/Cu values less than 7 in down-PSS5 and a medium-high value more than 10 in other PSSs (Fig. 7c). The ratio of vanadium to the sum of vanadium and nickel

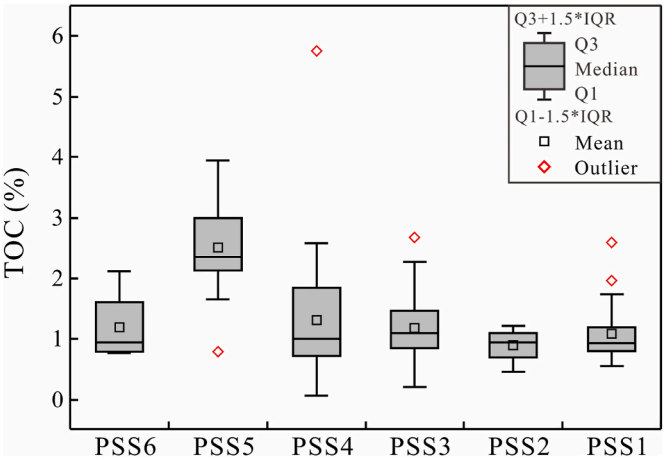

Fig. 4. Organic matter abundance of different PSSs in the E_1f^2 shale.

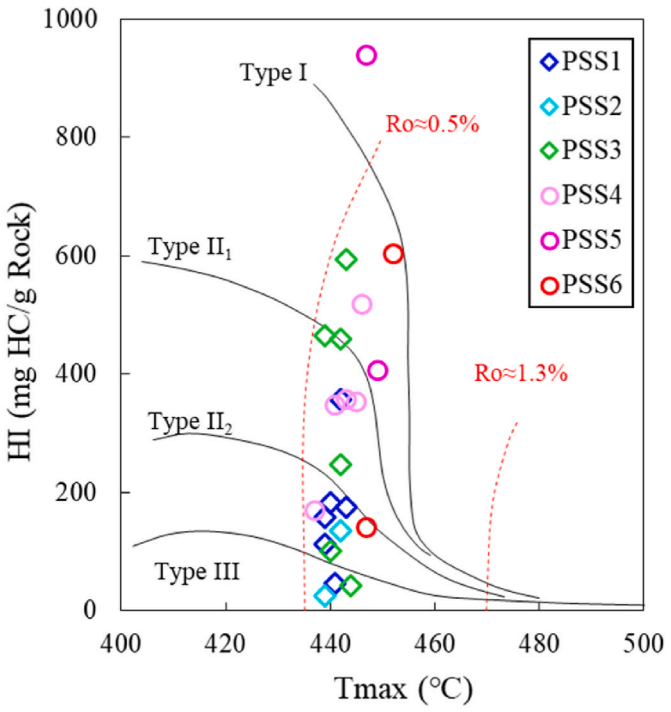

Fig. 5. Organic matter types of the E_1f^2 shale derived from Rock-eval parameters.

(V/(V + Ni)), an indicator for anoxia and euxinic conditions (Hatch and Leventhal, 1992), ranges from 0.6 to 0.8. The V/(V + Ni) values slightly decrease from 0.70 to 0.63 upward in PSS1 to PSS3 and demonstrate a positive shift in PSS4. It rapidly decreases in the transition of PSS4 and PSS5 and then gradually increases from 0.60 to 0.71 upward in PSS5 to PSS6 (Fig. 7e). The ratio of phosphorus to aluminum (P/Al) is a valuable proxy for bioproductivity by scaling P as a function of terrigenous content (Latimer et al., 2002; Algeo and Ingall, 2007). In PSS1 to mid-PSS4, the P/Al value is relatively low, ranging from 0.2 to 0.9 with an average of 0.3. From up-PSS4 to PSS6, it initially increases and then decreases, showing an inflection point at the maximum lake level (Fig. 7g). The ratio of manganese to strontium (Mn/Sr) is sensitive to diagenetic effects and has a range of 0.35–7.82, with an average of 1.36. Uranium (U) and molybdenum (Mo) are drastically impacted by the redox conditions of the water column, and therefore, they can be used to effectively constrain the paleoredox conditions (Robbins et al., 2016; Algeo and Li, 2020). The U_{EF} and Mo_{EF} values are 0.2–12.0 (avg. 1.9) and 1.2–13.6 (avg. 2.4), respectively (Supplementary Table 3).

4.4. Stable $\delta^{13}C$ and $\delta^{18}O$ isotopes

The organic carbon isotope ($\delta^{13}C_{org}$) values fluctuate from −25.8‰ to −28.6‰, with an average of −27.4‰. The $\delta^{13}C_{org}$ values decrease upward from PSS1 to PSS4 and then increase at PSS5 and PSS6 (Fig. 6a). The carbonate carbon isotope ($\delta^{13}C_{carb}$) values vary from −4.9‰ to 2.5‰, with an average of −0.8‰. The $\delta^{13}C_{carb}$ values gradually increase upward from PSS1 to mid-PSS5 and then slightly decrease from up-PSS5 to PSS6 (Fig. 7a). The negative $\delta^{13}C_{carb}$ excursion is observed in the PSS4-PSS6. The oxygen isotope ($\delta^{18}O$) values range from −9.8‰ to −2.8‰, with an average of −6.1‰ (Supplementary Table 4). The $\delta^{18}O$ values decrease upward (Fig. 7a).

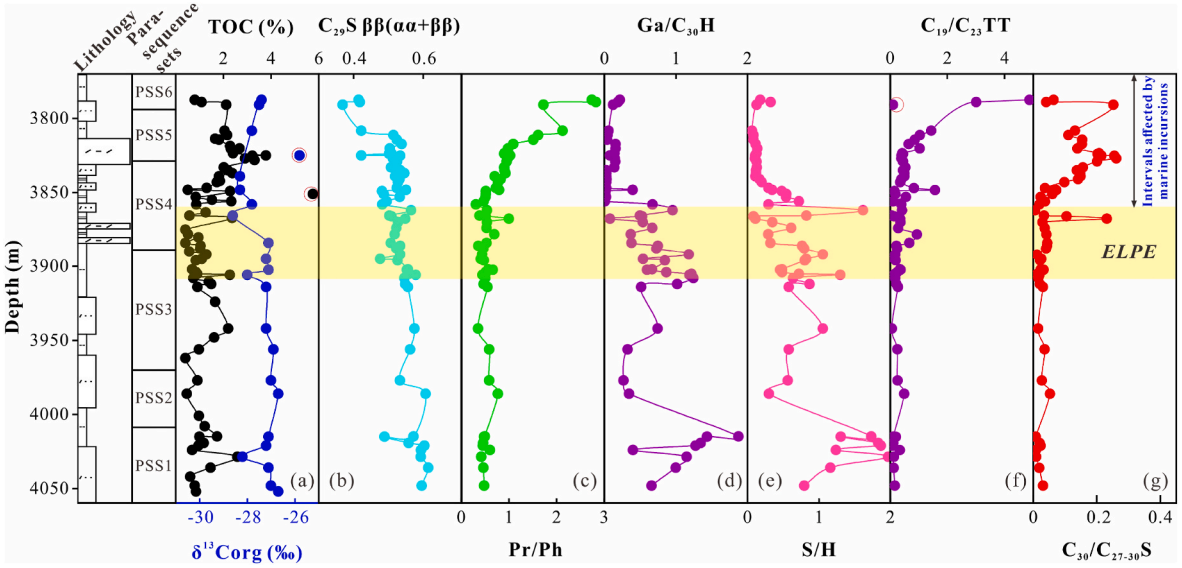

Fig. 6. Vertical variation of TOC, δ^{13}Corg, and biomarker parameters reflecting organic origins, terrestrial input, and paleoenvironment of the E_1f^2 shale.

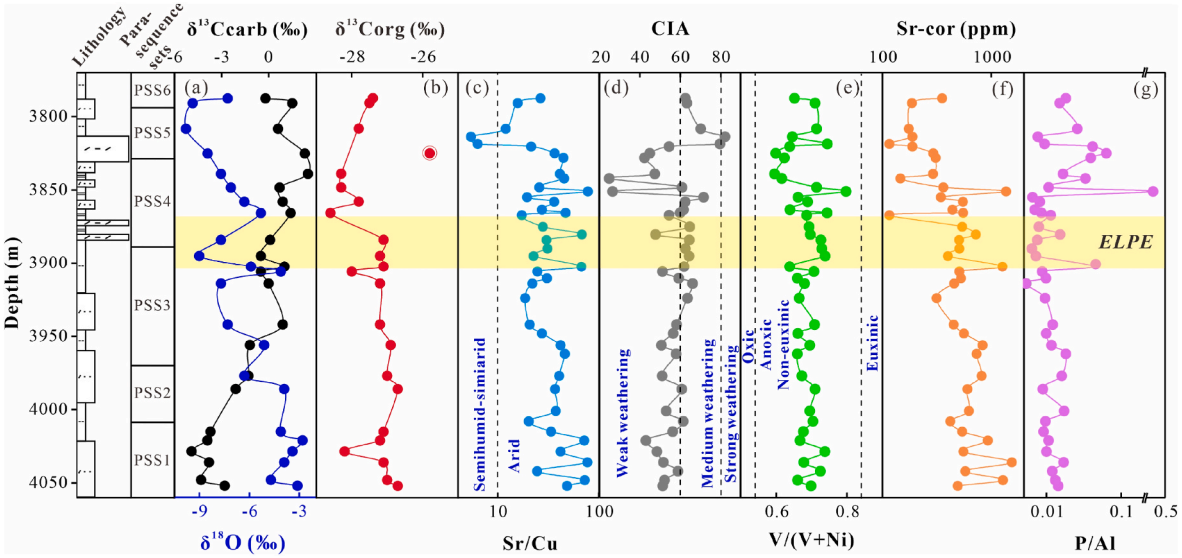

Fig. 7. The vertical variations of δ^{13}Ccarb, δ^{18}O, δ^{13}Corg, and element-geochemical proxies reflecting paleoclimate, paleosalinity, and paleoredox conditions of the E_1f^2 shale.

5. Discussion

5.1. Organic matter origins and seawater incursion identification

Organic matter type and thermal maturity are the main control of the petroleum generation and indirectly impact the biomarkers in sediments (Miceli Romero et al., 2018). The E_1f^2 shale is at the early stage of the oil window, with Tmax values of shale samples varying from 437 °C to 452 °C, with most of the samples having a vitrinite reflectance equivalent (R_{equ}) of 0.70–0.88 % (Supplementary Table 4), that as calculated from Tmax when considering specific organic matter types (Espitalié, 1986; Jarvie et al., 2001; Mastalerz and Drobniak, 2015; Evenick, 2021). The low R_{equ} and the C_{29}ββ/(αα+ββ) values less than the thermodynamic equilibrium value both support that thermal maturation of the E_1f^2 has little effect on biomarker signals for organic matter origin and paleoenvironment.

The 24-*n*-propylcholestanes are derived from two sterol precursors, 24-*n*-propylidene-cholesterols and 24-*n*-propylcholesterol, which are major sterol constituents of pelagophyte algae deposited in marine environments (Moldowan et al., 1990). The appearance of 24-*n*-propylcholestanes can be confirmed when the 4α-methyl-24-ethylcholestanes signal intensifies relative to the *m/z* 414 > 231 mass transition intensity exceeding 10 % (Xu et al., 2021; Ma et al., 2022). In the sample from a depth of 3825.05 m, the signal intensity of the *m/z* 414 > 217 relative to the *m/z* 414 > 231 is 15.3 % (Fig. 8). However, it is difficult to effectively identify the 24-*n*-propylcholestanes owing to the low abundance or the co-elution effects of C_{30} 4α-methyl-steranes (Moldowan, 1984; Xu et al., 2019). The ratio of C_{30} sterane to $C_{27\text{-}30}$ sterane ($C_{30}/C_{27-30}S$) can express the relative concentration of 24-*n*-propylcholestane and serve as a useful indicator for determining the extent of seawater incursions (Moldowan et al., 1985). The vertical variation of $C_{30}/C_{27-30}S$ is used to determine the intervals impacted by marine incursions. The aliphatic hydrocarbon chromatography of this study and that collected from the Zhejiang Oilfield are integrated to pinpoint the intervals impacted by marine incursions. The $C_{30}/C_{27-30}S$ values, notably below 0.1 % prior to the

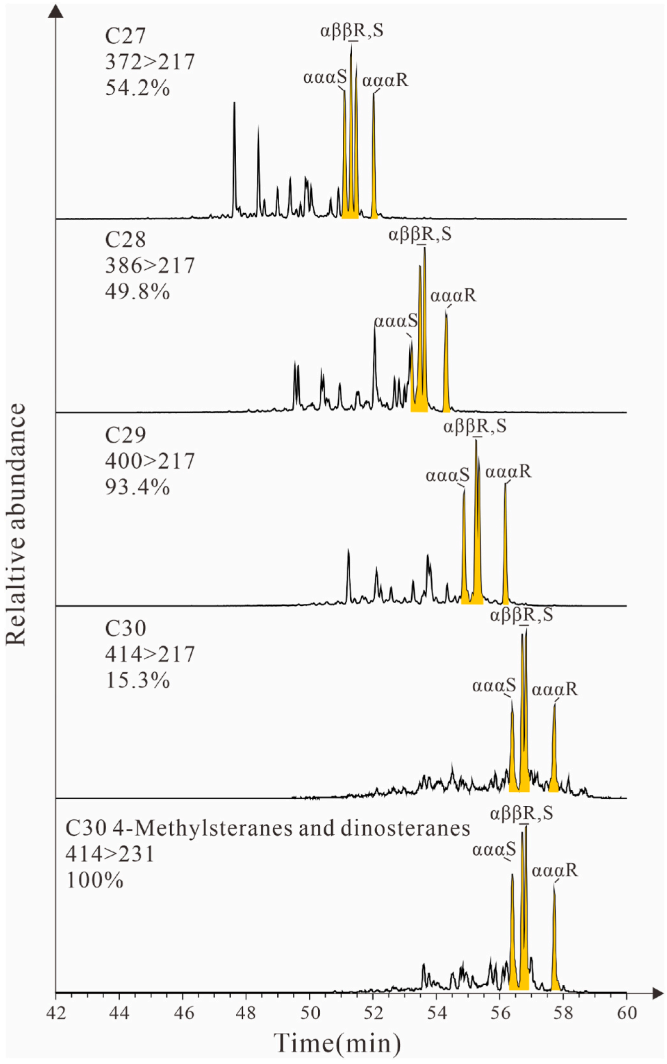

Fig. 8. MRM–GC–MS ion chromatograms of extractable C_{27}–C_{30} steranes from the E_1f^2 shale sample of the J19 Well at 3825.05 m demonstrating abundant steranes in E_1f^2 shale. The percentages express the relative signal intensity to that of C_{30} steranes for each sterane channel.

ELPE, surge above this threshold in the intervals of the PSS4, PSS5, and PSS6, signifying that these intervals were influenced by marine incursions. The higher $C_{30}/C_{27-30}S$ values indicate a stronger impact of marine incursions, with three peaks at about 4026.53 m (PSS6) in the J204 well, 3808.24–3841 m (PSS5), and 3866–3867.56 m (PSS4) in the J19 well (Fig. 6g).

The upward declining S/H values suggest a shift in primary OM contributors from eukaryotic organisms in PSS1 to down-PSS4 to prokaryotic bacteria dominance in up-PSS4 to PSS6. A power regression correlation between $C_{30}/C_{27-29}S$ and S/H reveals the significant influence of seawater incursions on organic matter origins. The values of $C_{30}S/C_{27-29}S$ exceeding 0.1 imply a significant impact of seawater incursions, corresponding to very low S/H values resulting from a predominance of prokaryotes in up-PSS4 to PSS6. The stronger the impact of seawater incursions, the more prokaryotes appear during this stage (Fig. 9a). A weak positive relationship between S/H and TOC in the PSS1-PSS3 suggests enhanced contributions from eukaryotes (Fig. 9b), such as algae, in response to arid suboxic saline-water conditions. In PSS4-PSS6, S/H values are relatively low, and the relationship between S/H and TOC becomes more complex (Fig. 9b), implying that the primary producers were bacteria and secondary contributions may arise from other organic origins.

Tricyclic terpanes have been widely used to discern organic matter origin and sedimentary environment (Wang and Simoneit, 1995; Ogbesejana et al., 2021). The low carbon number tricyclic terpanes ($C_{19\text{-}20}TT$) are primarily associated with diterpenoids, which are produced by higher plants (Zumberge, 1987). The C_{23} tricyclic terpanes ($C_{23}TT$) appear in marine or saline lake water conditions (Tao et al., 2015). The $C_{19}/C_{23}TT$ values are frequently used as a useful proxy for analyzing terrigenous organic matter input (Noble et al., 1986). The $C_{19}/C_{23}TT$ values keep stable low values with an average of 0.21 in PSS1-PSS3, which represents minimal terrigenous organic matter input. In contrast, the $C_{19}/C_{23}TT$ values of the PSS4-PSS6 are higher with an average of 0.7 and increase upward, which means an increase in runoff and terrigenous input during this period (Fig. 6f). Moreover, the highest $C_{19}/C_{23}TT$ values observed in the up-PSS5 and PSS6 may be related to the increasing terrigenous input during the high-stand system.

5.2. Paleoenvironmental reconstruction

5.2.1. Paleoclimate

The values of Sr/Cu, CIA, gallium to rubidium (Ga/Rb), potassium oxide to aluminium oxide (K_2O/Al_2O_3), were commonly used to reflect paleoclimate conditions (Roy and Roser, 2013; Xu et al., 2021). The Sr/Cu value is related to paleoclimate conditions, with values of <1, 1–10, and >10 reflecting humid, semihumid-semiarid, and arid

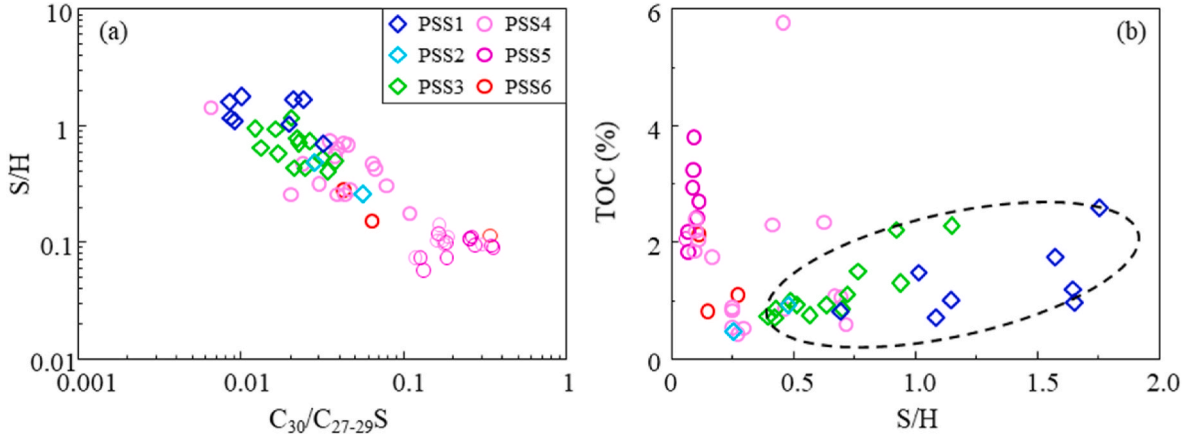

Fig. 9. Plot of $C_{30}/C_{27\text{-}29}S$ versus S/H implying a strong control of marine incursions on organic matter origins (a); and Plot of S/H versus TOC demonstrating the potential impact of different organic matter origins on TOC (b).

conditions, respectively (Xu et al., 2021). The relatively low Sr/Cu values in down-PSS5 and the medium-high values in other PSSs indicate an overall arid paleoclimate in the depositional period of the E_1f^2 shale, with a semihumid-semiarid climate nearing the maximum flooding level (Fig. 7c). The CIA is used to evaluate the paleoweathering intensity of fine-grained siliciclastic sediments (Xiao et al., 2020). Strong weathering is generally related to warm and humid conditions with CIA values exceeding 80, whereas weak weathering usually appears in cold and arid climates with CIA values less than 60 and CIA values of 60–80 reflecting moderate weathering conditions (Nesbitt and Young, 1982). The weak-to-medium weathering conditions are justified in E_1f^2 shale by the CIA range of 25~82 with an average of 57. The weakest weathering conditions are observed in proximity to the maximum flooding surface (Fig. 7d). Aluminum and gallium are mainly related to the fine-grained aluminosilicate fraction and tend to enrich in warm and humid climates (Hieronymus et al., 2001; Beckmann et al., 2005). Potassium and rubidium are associated with dry and cold climatic conditions and reflect chemical weathering (Ratcliffe et al., 2010). Therefore, high Ga/Rb values are correlated with decreasing aridity and rising temperature, whereas K_2O/Al_2O_3 values increase with increasing aridity and decreasing temperature (Roy and Roser, 2013). The K_2O/Al_2O_3–Ga/Rb plot demonstrates dry conditions for most of the E_1f^2 shale samples except individual samples in PSS1 and PSS4 (Fig. 10). Consequently, the E_1f^2 shale was primarily deposited under arid paleoclimate conditions with weak-medium weathering, and the weakest weathering occurred near the maximum flood surface.

5.2.2. Paleoredox conditions

The valence and solubility of redox-sensitive elements, such as V, U, and Mo, are closely associated with the redox conditions of the water column during the sedimentary period. Therefore, they can effectively help constrain paleoredox conditions (Robbins et al., 2016; Algeo and Li, 2020). When an oxidizing water column gradually becomes reducing, V in the form of soluble vanadate is reduced and easily precipitates into sediments (Wehrli and Stumm, 1989; Algeo and Maynard, 2004), whereas the competing metals, such as Ni, are effectively soluble in anoxic pore waters (Arthur and Sageman, 1994). Thus, V/(V + Ni) ratios can be employed as indicators for anoxia and euxinia (Hatch and Leventhal, 1992) and fall in the anoxic non-euxinic range for all E_1f^2 shale samples (Fig. 7e). A slight positive excursion of V/(V + Ni) in PSS4 means a somewhat reduced condition during this stage. Afterward, the redox conditions rapidly shifted toward slightly oxic conditions, progressively becoming more reducing from PSS5 to PSS6.

Uranium tends to be rich in sediments in the form of insoluble U^{4+} under highly reducing conditions. In contrast, U, as soluble U^{6+}, is released from sediments under oxidizing conditions (Algeo and Maynard, 2004; Tribovillard et al., 2006; Algeo and Tribovillard, 2009). Mo mainly exists as Mo^{6+} in oxic seawater and enriches in organic-rich sediments in the form of thiomolybdates under H_2S-rich euxinic reducing conditions (Zheng et al., 2000; Algeo and Maynard, 2004; Tribovillard et al., 2006; Algeo and Tribovillard, 2009). The patterns of molybdenum-uranium covariation are related to specific sedimentary attributes and depositional processes. Thus, the Mo_{EF}-U_{EF} covariation is used to assess the redox conditions of the E_1f^2 shale, indicating that the E_1f^2 shale is primarily deposited under suboxic conditions (Fig. 11). Redox conditions become subtle suboxic during the transition from PSS4 to PSS5.

5.2.3. Paleosalinity

The Sr concentration in sediments co-varies with waterbody salinity. It is more difficult to form chemical precipitation and is easily absorbed by clay and organic matter during the terrigenous detrital rock transportation from rivers to oceans (Wei and Algeo, 2020), leading to diverging Sr abundance among freshwater, brackish, and marine fields. Therefore, Sr concentration can work as a paleosalinity proxy. However, Sr substitutes easily for Ca^{2+} via filling lattice positions or occupying lattice defects in the carbonate mineral structure, which brings about higher Sr concentrations in sediments containing carbonate components (Brand and Veizer, 1980; Vahrenkamp and Swart, 1990; Wei and Algeo, 2020). The corrected Sr values (Sr-cor) after subtracting carbonate-host Sr are used to reflect the paleosanility (Wei et al., 2018). When Sr-cor values exceed 100 ppm, saline and hypersaline conditions are implied for the E_1f^2 shale (Quan et al., 2019; Wei and Algeo, 2020). These values gradually decrease upward from PPS1 to PSS5 and then increase in PSS6, suggesting that a rising lake level resulting from runoff might have decreased lake water salinity (Fig. 7f). The relatively high $Ga/C_{30}H$ ratios in PSS1 to down-PSS4 indicate water column stratification caused by high salinity in this period. In up-PSS4 to PSS6, $Ga/C_{30}H$ ratios are low (Fig. 6d), possibly related to seawater incursions and the increasing runoff. The inflow of marine water with high oxygen content may have disrupted water column stratification and disturbed the redox conditions at the lake bottom, leading to low $Ga/C_{30}H$ values.

5.2.4. Primary productivity

Phosphorus is a crucial nutrient for plankton in all environments and plays an important role in bioproductivity (Schindler, 1977). The

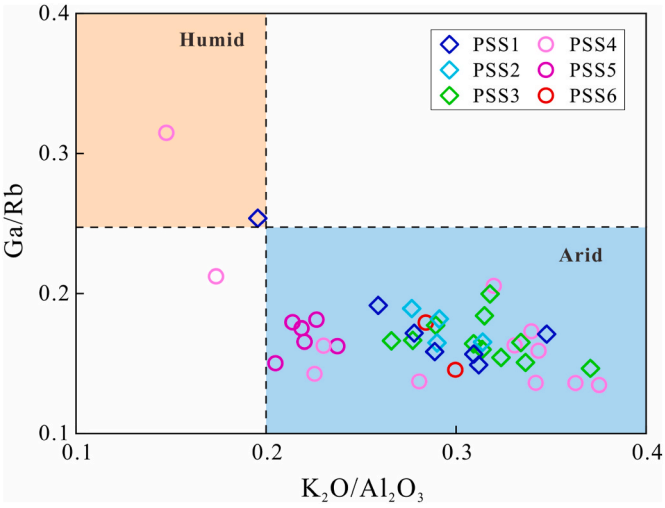

Fig. 10. The K_2O/Al_2O_3–Ga/Rb plot demonstrating the cool/dry conditions and weak-medium weathering for the E_1f^2 shale (The binary model from Roy and Roser (2013)).

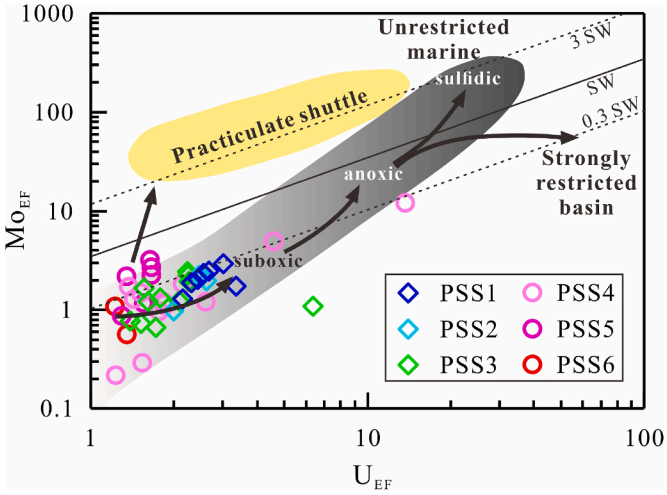

Fig. 11. Mo-TOC covariation for the E_1f^2 shale showing a restricted environment during the sedimentary period (The binary model from Algeo and Tribovillard (2009)).

absolute P fails to assess bioproductivity in light of terrigenous P supply, whereas the ratio of P to Al (P/Al) is a valuable proxy for bioproductivity by normalizing P as a function of terrigenous content (Latimer et al., 2002; Algeo and Ingall, 2007). In PSS1-PSS3, P/Al values are relatively low and show no significant relationship with TOC content (Fig. 12a), suggesting a secondary role of productivity in organic matter accumulation at this stage. However, in PSS4-PSS6, productivity plays a major role in organic matter accumulation, as indicated by the positive correlation between P/Al and TOC (Fig. 12b). The vertical variation of $C_{30}/C_{27-29}S$ is generally similar to that of P/Al (Figs. 6g and 7g), which perhaps implies that seawater incursions during PSS4-PSS6 brought nutrients and increased paleoproductivity.

5.3. A lacustrine response to the EPLE

The Early Paleogene experienced sustained global greenhouse warmth and dynamic climatic change with overall high global temperatures and transient climatic perturbations (Barnet et al., 2019). This period initially experienced relatively low temperatures from the early Paleocene to the mid-Paleocene, followed by an increase in temperature from the mid-Paleocene to the early Eocene (Zachos et al., 2001; Hollis et al., 2012), which is closely related to a series of abrupt environmental disruptions, including the Dan-C2 Event (~65.2 Ma), ELPE (~58.9 Ma), the peak-Paleocene Carbon Isotope Maximum Event (peak-PCIM, ~57.7 Ma), and the Palecene Eocene Thermal Maximum (PETM, ~55.5 Ma) (Zachos et al., 2001; Hollis et al., 2012; Barnet et al., 2019). The ELPE is an abrupt climate disruption accompanied by biological turnover, which has been reported in various geological records, including deep sea cores of the North Pacific and South Atlantic, marine sections of the western Pyrenees, and lacustrine outcrops in Spain and Argentina (Petrizzo, 2005; Bralower et al., 2006; Bernaola et al., 2007; Westerhold et al., 2008, 2011; Hyland et al., 2015; Coccioni et al., 2019). The ELPE represents a short global phenomenon that is located close to the top of the Chron C26r and lasts for 52–53 y.a. (Bernaola et al., 2007; Speijer et al., 2020). The deposition of the E_1f^2 shale occurred in the middle to late Paleocene (60.2–58 Ma), spanning C26r-C25r (Fig. 13) (Bernaola et al., 2007; Speijer et al., 2020). Thus, the ELPE indeed occurred in the deposition stage of the E_1f^2 and potentially impacted the depositional process of the E_1f^2 shale. This event is marked by the negative isotope excursion in $\delta^{18}O$ and $\delta^{13}C_{carb}$ of benthic foraminifer (Fig. 13a) (Cramer et al., 2009; Speijer et al., 2020), which can be pinpointed in the lacustrine E_1f^2 shale by comparing their $\delta^{13}Corg$, $\delta^{18}O$, and $\delta^{13}Ccarb$ trends. However, diagenetic effects need to first be evaluated before discussing chemostratigraphic correlation and environmental implications when using $\delta^{18}O$ values (Derry et al., 1994; Li et al., 2013). Carbonate samples with $\delta^{18}O$ values below −10 ‰ and Mn/Sr values exceeding 10 are considered to have an unacceptable diagenetic history (Kaufman and Knoll, 1995). The E_1f^2 has a minimum $\delta^{18}O$ value of −9.8 % and low Mn/Sr values less than 8, which supports the geochemical usefulness of the $\delta^{18}O$ values to pinpoint the ELPE. The ELPE is characterized by a 0.9 ‰ negative shift in $\delta^{13}Corg$, a 1.5 ‰ negative shift in $\delta^{13}Ccarb$, and a 3.7 ‰ negative excursion of $\delta^{18}O$ values in this case (Fig. 13e and f). All the above supports that the lacustrine E_1f^2 shale in Subei Basin has responses to the ELPE. In addition, the two-stage response to the ELPE in the terrestrial Cerro Bayo section is identified by two negative isotope excursions in $\delta^{13}C_{org}$, the increase in mean annual temperature, and the variation of phytolith assemblage compositions, which results from the rapid climatic change and brings about changes in vegetation composition and diversity (Hyland et al., 2015). It implies that the lacustrine deposition system might have a more complex response to the ELPE. Similarly, the geochemistry proxy fluctuation, such as Ga/C_{30} H and S/H ratio, suggests the possibility of multistage ELPE in the E_1f^2 shale deposition, potentially related to orbital climate cycles.

The ELPE, corresponding to relatively low temperatures, slightly elevated atmospheric CO_2, and low sea levels (Fig. 13b–d), represents a major shift in climate boundary conditions from a cooling regime to a long-term warming phase during mid-Paleocene to late Paleocene (Fig. 13c) (Hollis et al., 2012). This shift is believed to have caused changes in the plankton assemblage in the Zumaia section, which is closely associated with the disturbed environment that impacts the water column temperature and mesotrophic/oligotrophic conditions (Zachos et al., 2005). It subsequently follows a gradually increasing temperature and triggers a rising sea level globally (Fig. 13b) (Littler et al., 2014), providing opportunities for marine invasions into coastal lacustrine basins. The Subei Basin, part of the continental area in the North Jiangsu-South Yellow Sea Basin, adjoined the ancient East China Sea from the Cretaceous to the Tertiary. The differential subsidence of the basin coupled with the rising sea level of the ancient East China Sea during this period created the conditions for marine incursions into the Subei Basin (Fu et al., 2007). The increasing extent of marine incursions usually brings about higher primary productivity (Xia et al., 2019). Sea water from the ancient East China Sea influxes into the Subei Basin along some broken valley gaps, potentially introducing nutrients, enhancing primary productivity, affecting lake water chemistry and circulation patterns, and driving biotic community variation (Santos et al., 2008; Marzocchi et al., 2016; Virtasalo et al., 2016; Song et al., 2021). These have a knock-on effect on biodiversity, ecosystems, and depositional processes for the E_1f^2 shale, which is potentially favorable to organic matter accumulation. The E_1f^2 shale serves as a unique stratigraphic

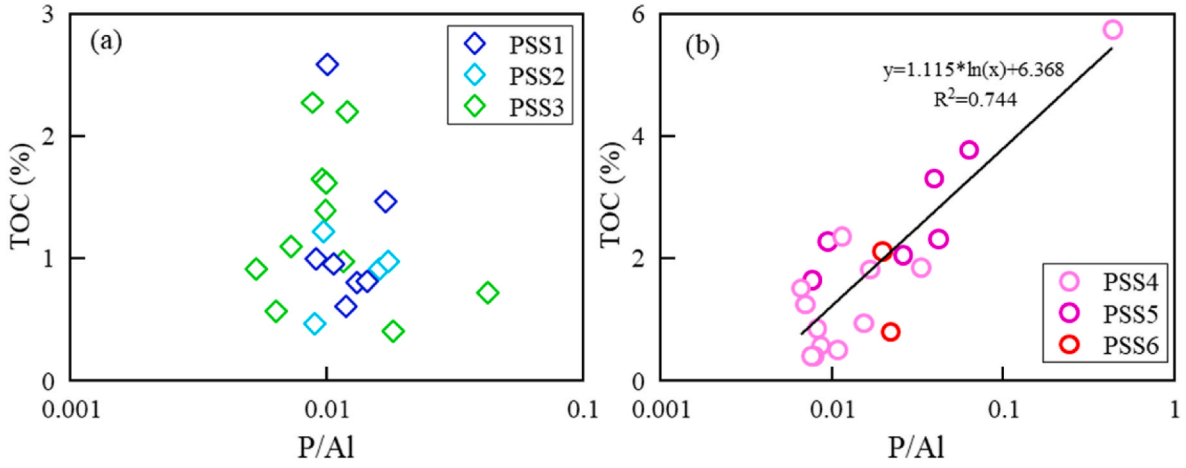

Fig. 12. The plots of P/Al and TOC demonstrating the impact of productivity on organic matter abundance: the change in P/Al values has little to do with TOC values during PSS1-PSS3 (a); and the improved P/Al values increase TOC (b).

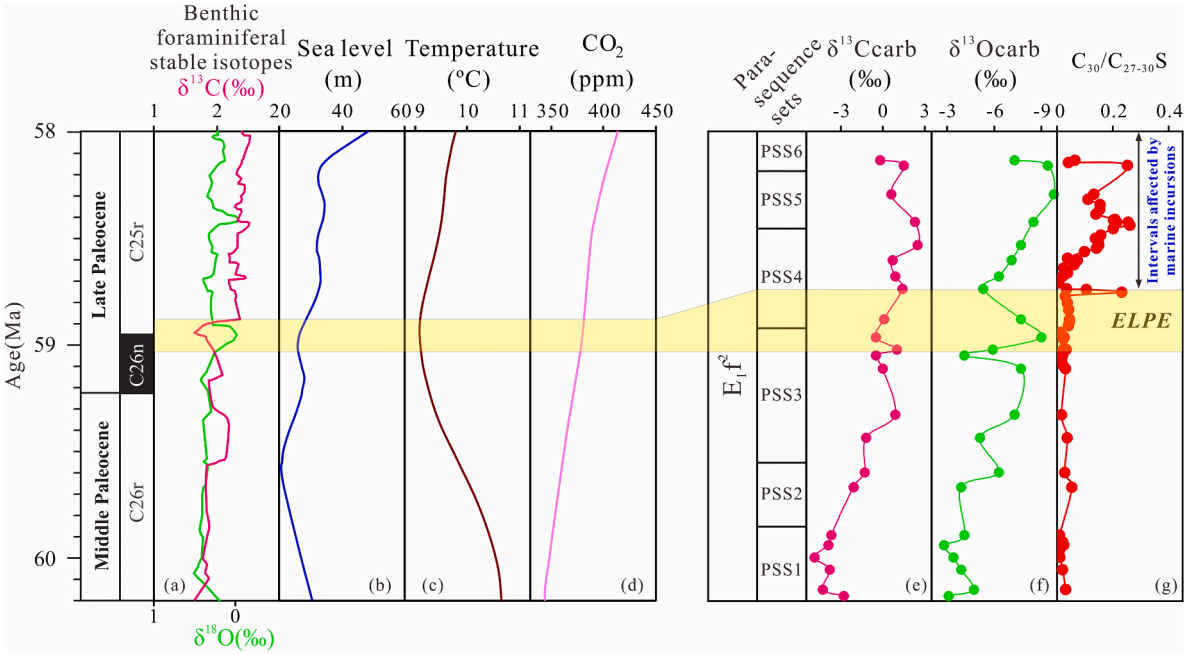

Fig. 13. Comparison of the stable isotopic signature of the ELPE between the E_1f^2 shale and deep-water benthic foraminifera (Cramer et al., 2009). The light-yellow zone represents the period of the ELPE. The global atmosphere *p*CO2 and the temperature curve obtained from Beerling and Royer (2011) and the sea level variation obtained from benthic foraminiferal $\delta^{18}O$ splice (Miller et al., 2020).

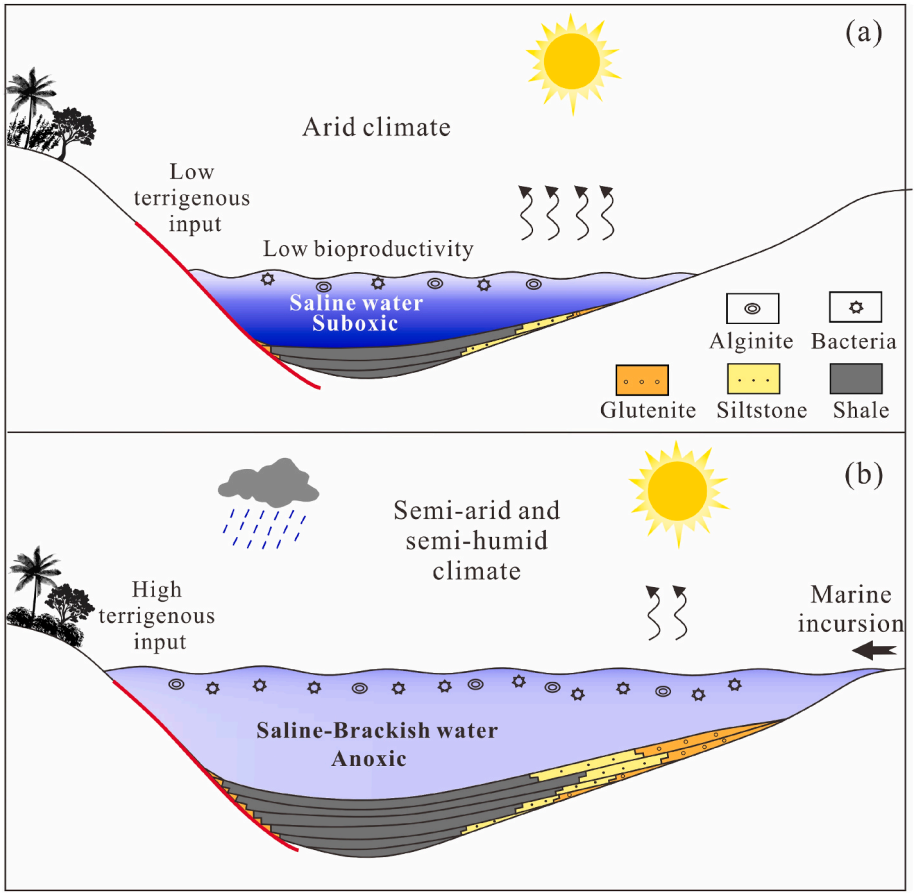

Fig. 14. Organic matter accumulation models of the E_1f^2 shale in the Subei Basin for different depositional stages: PSS1-PSS3 (a); and PSS4-PSS6 (b).

record to correlate regional depositional processes with ELPE. This period also provides a valuable window for investigating the impact of threshold events in the climate system in response to gradual changes in boundary conditions (Littler et al., 2014).

5.4. Organic matter accumulation

Prior to the ELPE, the arid paleoclimate in the Subei Basin decreased the runoff and increased evaporation, potentially inducing a saline water column and favoring the proliferation of some salt-tolerant eukaryotic producers. Less bioavailable nutrients are available because of the decreasing runoff, the resulting saline environment narrows biodiversity and is favorable to specific biological populations. The type II_2 organic matter dominated during this stage, with some type II_1 and type III kerogen (Fig. 5). Eukaryotic primary producers were the major contributors to sedimentary organic matter during this stage, and the relatively poor organic matter accumulation might be related to the low primary productivity (Fig. 14a). The ELPE is located at the top of PSS3 and the bottom of PSS4. The E_1f^2 shale is deposited in an arid and saline water condition with anoxic and medium weathering at this stage. The obvious climate variation might be related to orbital climate cycles, potentially inducing multi-stage change in the biotic community. This period served as an inflection point and initialized the marine incursions into the Subei Basin. Following the ELPE, the rising sea level potentially induced the marine invasion into the lacustrine basin, and the arid to semi-arid or semi-humid paleoclimate increased runoff and lake level, especially for the boundary between PSS4 and PSS5. That resulted in the mixing of the lake and marine water from up-PSS4 to PSS6. The relatively higher primary productivity might be interpreted by the introduction of bioavailable nutrient elements from marine water and runoff, which further promoted organic matter enrichment and high TOC. Oil-prone organic matter predominates during this stage, with most samples consisting of type I and II of organic matter (Fig. 5). Prokaryotes were the main primary producers, with secondary contributions of other origins due to the mixture of marine and lake water at this stage, such as marine algae (24-*n*-propylcholestanes) and lacustrine higher plants (abundant low carbon number of tricyclic terpanes) (Fig. 14b). Overall, the global ELPE impacted the lacustrine E_1f^2 shale deposition processes, and the subsequent marine incursions potentially promoted organic matter accumulation in the lacustrine system.

6. Conclusions

The lacustrine response to the ELPE and subsequent marine incursions have been found in the E_1f^2 shale of the Subei Basin, demonstrating the impact of global climatic turbulence on the lacustrine shale deposition process and organic matter accumulation.

The interval of PSS1 to down-PSS3 deposited prior to the ELPE has relatively low TOC values. The decrease in runoff related to the arid paleoclimate during this period decreased the bioavailable nutrient influx. The resulting saline water column restricted biodiversity, with eukaryotic primary producers playing a significant role in organic matter enrichment at this stage. At the deposition period of up-PSS3 to down-PSS4, the ELPE occurred and was recorded by a 1.5‰ negative shift in $\delta^{13}C_{carb}$ and a 3.7‰ negative excursion of $\delta^{18}O$ values in the E_1f^2 shale. The subsequently increasing temperature and rising global sea level brought about intermittent marine incursions into the Subei Basin, which have been identified by the appearance of 24-*n*-propylcholestane and $C_{30}/C_{27-29}S$ in the depositional period of up-PSS4 to PSS6. The intervals of up-PSS4 to PSS6 with relatively high TOC values experienced an arid to semihumid-semiarid climate and a saline to brackish waterbody. Marine incursions potentially introduced additional nutrients and improved primary productivity, as indicated by the consistency between $C_{30}/C_{27-29}S$ and P/Al. Organic matter of different origins makes contributions to organic matter accumulation, with the predominance of eukaryotic primary producers. The E_1f^2 shale is a high hydrocarbon generation interval as the potential shale oil exploration target and provides an archive for the precise correlation of regional depositional processes with global climate events.

CRediT authorship contribution statement

Ming Guan: Writing – review & editing, Writing – original draft, Investigation, Data curation, Conceptualization. **Xiaoping Liu:** Supervision, Funding acquisition. **Zhijun Jin:** Supervision. **Wenzhi Zhao:** Supervision. **Wei Liu:** Writing – review & editing. **Leibo Bian:** Methodology, Investigation. **Jin Dong:** Validation, Project administration. **Xu Zeng:** Validation, Formal analysis. **Bang Zeng:** Methodology, Data curation. **Biao Sun:** Visualization. **Hanxi Liu:** Visualization, Data curation. **Zibin Wang:** Data curation.

Declaration of competing interest

The authors declare that they have no known competing financial interests or personal relationships that could have appeared to influence the work reported in this paper.

Data availability

Data will be made available on request.

Acknowledgements

This work was funded by the National Natural Science Foundation of China (Grant numbers 42072150 and U22B6004) and the PetroChina Research Institute of Petroleum Exploration and Development (Grant numbers 2022yjcq03). We thank PetroChina Zhejing Oilfield Company for their support. We appreciate the enthusiastic support of Weilai Zhang at the China University of Petroleum-Beijing and Huiyuan Xu at the SINOPEC Exploration and Development Research Institute for marine origin biomarker identification. We acknowledge Dr. Barry J. Katz and two anonymous reviewers for their valuable comments and suggestions, which greatly improved the manuscript of an earlier version.

Appendix A. Supplementary data

Supplementary data to this article can be found online at https://doi.org/10.1016/j.marpetgeo.2024.106730.

References

Algeo, T.J., Ingall, E., 2007. Sedimentary Corg: P ratios, paleocean ventilation, and Phanerozoic atmospheric pO2. Palaeogeogr. Palaeoclimatol. Palaeoecol. 256 (3–4), 130–155.
Algeo, T.J., Li, C., 2020. Redox classification and calibration of redox thresholds in sedimentary systems. Geochem. Cosmochim. Acta 287, 8–26.
Algeo, T.J., Maynard, J.B., 2004. Trace-element behavior and redox facies in core shales of Upper Pennsylvanian Kansas-type cyclothems. Chem. Geol. 206 (3–4), 289–318.
Algeo, T.J., Tribovillard, N., 2009. Environmental analysis of paleoceanographic systems based on molybdenum-uranium covariation. Chem. Geol. 268 (3–4), 211–225.
Arthur, M.A., Sageman, B.B., 1994. Marine black shales: depositional mechanisms and environments of sncient deposits. Annu. Rev. Earth Planet Sci. 22 (1), 499–551.
Barnet, J.S.K., Littler, K., Westerhold, T., Kroon, D., Leng, M.J., Bailey, I., Roehl, U., Zachos, J.C., 2019. A high-fidelity benthic stable isotope record of Late Cretaceous-early Eocene climate change and carbon-cycling. Paleoceanogr. Paleoclimatol. 34 (4), 672–691.
Beckmann, B., Flögel, S., Hofmann, P., Schulz, M., Wagner, T., 2005. Orbital forcing of Cretaceous river discharge in tropical Africa and ocean response. Nature 437 (7056), 241–244.
Beerling, D.J., Royer, D.L., 2011. Convergent cenozoic CO2 history. Nat. Geosci. 4 (7), 418–420.
Bernaola, G., Baceta, J.I., Orue-Etxebarria, X., Alegret, L., Martin-Rubio, M., Arostegui, J., Dinares-Turell, J., 2007. Evidence of an abrupt environmental disruption during the mid-Paleocene biotic event (Zumaia section, western Pyrenees). Geol. Soc. Am. Bull. 119 (7–8), 785–795.
Bralower, T.J., Silva, I.P., Malone, M.J., 2006. Leg 198 synthesis: a remarkable 120-m.y. record of climate and oceanography from Shatsky Rise, northwest Pacific Ocean. Proc. Ocean Drill. Progr. Sci. Results 198.

Brand, U., Veizer, J., 1980. Chemical diagenesis of a multicomponent carbonate system; 1, Trace elements. J. Sediment. Petrol. 50 (4), 1219–1236.
Chen, A., 2010. Tectonic features of the Subei Basin and the forming mechanism of its dustpan-shaped fault depression. Oil Gas Geol. 31 (2), 140–150.
Chen, L., Lu, Y., Jiang, S., Li, J., Guo, T., Luo, C., 2015. Heterogeneity of the lower silurian longmaxi marine shale in the southeast sichuan basin of China. Mar. Petrol. Geol. 65, 232–246.
Coccioni, R., Frontalini, F., Catanzariti, R., Jovane, L., Rodelli, D., Rodrigues, I.M.M., Savian, J.F., Giorgioni, M., Galbrun, B., 2019. Paleoenvironmental signature of the selandian-thanetian transition event (STTE) and early late Paleocene event (ELPE) in the contessa road section (western neo-tethys). Palaeogeogr. Palaeoclimatol. Palaeoecol. 523, 62–77.
Cramer, B.S., Toggweiler, J.R., Wright, J.D., Katz, M.E., Miller, K.G., 2009. Ocean overturning since the Late Cretaceous: inferences from a new benthic foraminiferal isotope compilation. Paleoceanography 24, PA4216.
Demaison, G.J., Moore, G.T., 1980. Anoxic environments and oil source bed genesis. Org. Geochem. 2 (1), 9–31.
Derry, L.A., Brasier, M.D., Corfield, R.M., Rozanov, A.Y., Zhuravlev, A.Y., 1994. Sr and C isotopes in Lower Cambrian carbonates from the Siberian Craton: A paleoenvironmental record during the 'Cambrian explosion'. Earth Planet Sci. Lett. 128 (3–4), 671–681.
Evenick, J.C., 2021. Examining the relationship between Tmax and vitrinite reflectance: an empirical comparison between thermal maturity indicators. J. Nat. Gas Sci. Eng. 91, 103946.
Espitalié, J., 1986. Use of Tmax as a maturation index for different types of organic matter comparison with vitrinite reflectance. In: Burrus, J. (Ed.), Thermal Modeling in Sedimentary Basins: Paris. E′ditions Technip, pp. 475–496.
Fu, Q., Li, Y., Zhang, G., Liu, Y., 2007. Evidence of transgression lake of Subei Basin during late cretaceous and Paleocene epoch and its geological significance. Acta Sedmentary Sinica 25 (3), 380–385.
Grantham, P.J., 1986. Sterane isomerisation and moretane/hopane ratios in crude oils derived from Tertiary source rocks. Org. Geochem. 12 (6), 495–506.
Guan, M., Liu, X., Jin, Z., Lai, J., Liu, J., Sun, B., Liu, T., Hua, Z., Xu, W., Shu, H., Wang, G., Liu, M., Luo, Y., 2022. Quantitative characterization of various oil contents and spatial distribution in lacustrine shales: insight from petroleum compositional characteristics derived from programed pyrolysis. Mar. Petrol. Geol. 138, 105522.
Hatch, J.R., Leventhal, J.S., 1992. Relationship between inferred redox potential of the depositional environment and geochemistry of the upper pennsylvanian (missourian) Stark shale member of the dennis limestone, wabaunsee county, Kansas. U.S.A. Chemical Geology 99, 65–82.
Hieronymus, B., Kotschoubey, B., Boulegue, J., 2001. Gallium behaviour in some contrasting lateritic profiles from Cameroon and Brazil. J. Geochem. Explor. 72 (2), 147–163.
Hollis, C.J., Taylor, K.W.R., Handley, L., Pancost, R.D., Huber, M., Creech, J.B., Hines, B. R., Crouch, E.M., Morgans, H.E.G., Crampton, J.S., Gibbs, S., Pearson, P.N., Zachos, J.C., 2012. Early Paleogene temperature history of the Southwest Pacific Ocean; reconciling proxies and models. Earth Planet Sci. Lett. 349–350, 53–66.
Hoyle, T.M., Leroy, S.A.G., López-Merino, L., van Baak, C.G.C., Martínez Cortizas, A., Richards, K., Aghayeva, V., 2021. Biological turnovers in response to marine incursion into the Caspian Sea at the Plio-Pleistocene transition. Global Planet. Change 206, 103623.
Huc, A.Y., Durand, B., Roucachet, J., Vandenbroucke, M., Pittion, J.L., 1986. Comparison of three series of organic matter of continental origin. Org. Geochem. 10 (1–3), 65–72.
Hyland, E.G., Sheldon, N.D., Cotton, J.M., 2015. Terrestrial evidence for a two-stage mid-Paleocene biotic event. Palaeogeogr. Palaeoclimatol. Palaeoecol. 417, 371–378.
Ilgen, A.G., Heath, J.E., Akkutlu, I.Y., Bryndzia, L.T., Cole, D.R., Kharaka, Y.K., Kneafsey, T.J., Milliken, K.L., Pyrak-Nolte, L.J., Suarez-Rivera, R., 2017. Shales at all scales: exploring coupled processes in mudrocks. Earth Sci. Rev. 166, 132–152.
Jarvie, D.M., Claxton, B.L., Henk, F., Breyer, J.T., 2001. Oil and shale gas from the barnett shale, ft. In: AAPG Annual Meeting, Denver, Colorado. Worth Basin, Texas.
Kaufman, A.J., Knoll, A.H., 1995. Neoproterozoic variations in the C-isotopic composition of seawater: stratigraphic and biogeochemical implications. Precambrian Res. 73, 27–49.
Keller, G., 2005. Impacts, volcanism and mass extinction: random coincidence or cause and effect? J. Geol. Soc. Aust. 52 (4–5), 725–757.
Kuypers, M., Pancost, R.D., Nijenhuis, I.A., Sinninghe Damsté, J.S., 2002. Enhanced productivity led to increased organic carbon burial in the euxinic North Atlantic basin during the late Cenomanian oceanic anoxic event. Paleoceanogr. Paleoclimatol. 17 (4), 3-1-3-13.
Latimer, J.C., Filippelli, G.M., Gersonde, R., Hodell, D.A., 2002. Eocene to Miocene terrigenous inputs and export production; geochemical evidence from ODP Leg 177, Site 1090. Palaeogeogr. Palaeoclimatol. Palaeoecol. 182 (3–4), 151–164.
Li, D., Ling, H., Shields-Zhou, G.A., Chen, X., Cremonese, L., Och, L., Thirlwall, M., Manning, C.J., 2013. Carbon and strontium isotope evolution of seawater across the ediacaran–cambrian transition: evidence from the xiaotan section, NE yunnan, South China. Precambrian Res. 225, 128–147.
Li, S., Zhao, G., Dai, L., Zhou, L., Liu, X., Suo, Y., Santosh, M., 2012. Cenozoic faulting of the Bohai Bay Basin and its bearing on the destruction of the eastern north China craton. J. Asian Earth Sci. 47, 80–93.
Littler, A.K., Rhl, B.U., Westerhold, B.T., Zachos, A.J.C., 2014. A high-resolution benthic stable-isotope record for the South Atlantic: implications for orbital-scale changes in Late Paleocene–Early Eocene climate and carbon cycling. Earth Planet Sci. Lett. 401 (10), 18–30.
Liu, W., Liu, M., Yang, T., Liu, X., Them, T.R., Wang, K., Bian, C., Meng, Q., Li, Y., Zeng, X., 2022. Organic matter accumulations in the santonian-campanian (upper cretaceous) lacustrine Nenjiang shale (K2n) in the Songliao Basin, NE China: terrestrial responses to OAE3? Int. J. Coal Geol. 260.
Liu, X., Lai, J., Fan, X., Shu, H., Wang, G., Ma, X., Liu, M., Guan, M., Luo, Y., 2020. Insights in the pore structure, fluid mobility and oiliness in oil shales of Paleogene Funing Formation in Subei Basin, China. Mar. Petrol. Geol. 114, 104228.
Liu, Y., Chen, Q., Wang, X., Hu, K., Cao, S., Wu, L., Gao, F., 2017. Influence of normal fault growth and linkage on the evolution of a rift basin: a case from the Gaoyou depression of the Subei Basin, eastern China. AAPG (Am. Assoc. Pet. Geol.) Bull. 101 (2), 265–288.
Ma, J., Wu, C., Uveges, B.T., Ding, W., Summons, R.E., Cui, X., 2022. Biomarkers reveal Eocene marine incursions into the Qaidam Basin, north Tibetan plateau. Org. Geochem. 166, 104380.
Marzocchi, A., Flecker, R., van Baak, C.G.C., Lunt, D.J., Krijgsman, W., 2016. Mediterranean outflow pump: an alternative mechanism for the Lago-mare and the end of the Messinian salinity crisis. Geology (Boulder) 44 (7), 523–526.
Mastalerz, M., Drobniak, A., 2015. Thermal alteration index (TAI), vitrinite reflectance, and Tmax through maturation. In: The 32nd Annual Meeting of the Society for Organic Petrology. Yogyakarta, Java, Indonesia.
Mclennan, S.M., Hemming, S., Mcdaniel, D.K., Hanson, G.N., 1993. Geochemical approaches to sedimentation, provenance, and tectonics. Processes controlling the composition of clastic sediments. Geological Sociaty of America 284, 21–34.
Miller, K.G., Browning, J.V., Schmelz, W.J., Kopp, R.E., Mountain, G.S., Wright, J.D., 2020. Cenozoic sea-level and cryospheric evolution from deep-sea geochemical and continental margin records. Sci. Adv. 6 (20) eaaz1346.
Moldowan, J.M., 1984. C30-steranes, novel markers for marine petroleums and sedimentary rocks. Geochem. Cosmochim. Acta 48 (12), 2767–2768.
Moldowan, J.M., Fago, F.J., Lee, C.Y., Jacobson, S.R., Watt, D.S., Slougui, N., Jeganathan, A., Young, D.C., 1990. Sedimentary 24-n-Propylcholestanes, molecular fossils diagnostic of marine algae. Science (American Association for the Advancement of Science) 247 (4940), 309–312.
Moldowan, J.M., Seifert, W.K., Gallegos, E.J., 1985. Relationship between petroleum composition and depositional environment of petroleum source rocks. AAPG (Am. Assoc. Pet. Geol.) Bull. 69 (8), 1255–1268.
Nesbitt, H.W., Young, G., 1982. Early Proterozoic climates and plate motions inferred from major element chemistry of lutites. Nature 299 (5885), 715–717.
Noble, R.A., Alexander, R., Kagi, R.I., Knox, J., Leythaeuser, D., Rullkoetter, J., 1986. Identification of some diterpenoid hydrocarbons in petroleum. Org. Geochem. 10 (4–6), 825–829.
Ogbesejana, A.B., Bello, O.M., Ali, T., Uduma, U.A., Kabo, K.S., Akintade, O.O., 2021. Geochemical significance of tricyclic and tetracyclic terpanes in source rock extracts from the Offshore Niger Delta Basin, Nigeria. Acta Geochimica 40 (2), 184–198.
Petrizzo, M.R., 2005. An early late Paleocene event on shatsky rise, northwestern pacific ocean (ODP leg 198) evidence from planktonic foraminiferal assemblages. Proc. Ocean Drill. Progr. Sci. Results 198.
Quan, Y., Liu, J., Hao, F., Cai, Z., Xie, Y., 2019. Paleosalinity assessment and its influence on source rock deposition in the western pearl river mouth basin, South China sea. Geol. Soc. Am. Bull. 132 (7–8).
Ran, H., Si, B., Chen, B., Fan, L., 2012. Sedimentary sequences in haian depression and control on reservoir of the Paleocene. Oil Geophys. Prospect. 47 (5), 795-802+844+681.
Ratcliffe, K.T., Wright, A.M., Montgomery, P., Palfrey, A., Vonk, A., Vermeulen, J., Barrett, M., 2010. Application of chemostratigraphy to the mungaroo formation, the gorgon field, offshore northwest Australia. APPEA J. Aust. Pet. Prod. Explor. Assoc. 50 (1), 371–388.
Rimmer, S.M., Thompson, J.A., Goodnight, S.A., Robl, T.L., 2004. Multiple controls on the preservation of organic matter in Devonian–Mississippian marine black shales: geochemical and petrographic evidence. Palaeogeogr. Palaeoclimatol. Palaeoecol. 215 (1–2), 125–154.
Rimstidt, J.D., Chermak, J.A., Schreiber, M.E., 2017. Processes that control mineral and element abundances in shales. Earth Sci. Rev. 171, 383–399.
Robbins, L.J., Lalonde, S.V., Planavsky, N.J., Partin, C.A., Reinhard, C.T., Kendall, B., Scott, C., Hardisty, D.S., Gill, B.C., Alessi, D.S., Dupont, C.L., Saito, M.A., Crowe, S. A., Poulton, S.W., Bekker, A., Lyons, T.W., Konhauser, K.O., 2016. Trace elements at the intersection of marine biological and geochemical evolution. Earth Sci. Rev. 163, 323–348.
Romero Miceli, A.A., Nguyen, T., Philp, Paul R., 2018. Organic geochemistry of the eagle ford group in Texas. AAPG (Am. Assoc. Pet. Geol.) Bull. 102 (7), 1379–1412.
Ross, D.J.K., Bustin, R.M., 2009. Investigating the use of sedimentary geochemical proxies for paleoenvironment interpretation of thermally mature organic-rich strata: examples from the Devonian–Mississippian shales, Western Canadian Sedimentary Basin. Chem. Geol. 260 (1–2), 1–19.
Roy, D.K., Roser, B.P., 2013. Climatic control on the composition of carboniferous–permian gondwana sediments, khalaspir basin, Bangladesh. Gondwana Res. 23 (3), 1163–1171.
Santos, C., Jaramillo, C., Bayona, G., Rueda, M., Torres, V., 2008. Late Eocene marine incursion in north-western South America. Palaeogeogr. Palaeoclimatol. Palaeoecol. 264 (1–2), 140–146.
Schindler, D.W., 1977. Evolution of phosphorus limitation in lakes. Science 195 (4275), 260–262.
Seifert, W.K., Moldowan, J.M., 1986. Use of biological markers in petroleum exploration. In: Johns, R.B. (Ed.), Methods in Geochemistry and Geophysics, vol. 24, pp. 61–290.
Sepúlveda, J., Wendler, J., Leider, A., Kuss, H., Summons, R.E., Hinrichs, K., 2009. Molecular isotopic evidence of environmental and ecological changes across the

Cenomanian–Turonian boundary in the Levant Platform of central Jordan. Org. Geochem. 40 (5), 553–568.
Shu, L., Wang, B., Wang, L., He, G., 2005. Analysis of northern Jiangsu prototype basin from late cretaceous to Neogene. Geol. J. China Univ. 11 (4), 534–543.
Sinninghe Damsté, J., Keely, B.J., Betts, S.E., Baas, M., Maxwell, J.R., Leeuw, J., 1993. Variations in abundances and distributions of isoprenoid chromans and long-chain alkylbenzenes in sediments of the Mulhouse Basin: a molecular sedimentary record of palaeosalinity. Org. Geochem. 20 (8), 1201–1215.
Smith, M.P., Harper, D.A.T., 2013. Causes of the cambrian explosion. Science 341 (6152), 1355–1356.
Song, Y., Cao, Q., Li, S., Hu, S., Zhu, K., Ye, X., Wan, L., 2021. Salinized lacustrine organic-rich shale influenced by marine incursions; algal-microbial community, paleoenvironment and shale oil potential in the Paleogene Biyang Depression, east China. Palaeogeogr. Palaeoclimatol. Palaeoecol. 580, 110621.
Speijer, R.P., Pälike, H., Hollis, C.J., Hooker, J.J., Ogg, J.G., 2020. Chapter 28 - the Paleogene Period. Geologic Time Scale. Elsevier, pp. 1087–1140.
Su, A., Chen, H., Feng, Y.X., Zhao, J., 2022. LA-ICP-MS U-Pb dating and geochemical characterization of oil inclusion-bearing calcite cements: constraints on primary oil migration in lacustrine mudstone source rocks. Geol. Soc. Am. Bull. 134 (7/8), 2022–2036.
Tao, S., Wang, C., Du, J., Liu, L., Chen, Z., 2015. Geochemical application of tricyclic and tetracyclic terpanes biomarkers in crude oils of NW China. Mar. Petrol. Geol. 67, 460–467.
Taylor, S.R., McLennan, S.M., 1985. The Continental Crust: its Composition and Evolution. Blackwell Scientific Publications, United States.
Tribovillard, N., Algeo, T.J., Lyons, T., Riboulleau, A., 2006. Trace metals as paleoredox and paleoproductivity proxies: an update. Chem. Geol. 232 (1–2), 12–32.
Tyson, R.V., 2005. The "productivity versus preservation" controversy: cause, flaws, and resolution. Deposition of Organic-Carbon-Rich Sediments: models. Society for Sedimentary Geology 17–33.
Vahrenkamp, V.C., Swart, P.K., 1990. New distribution coefficient for the incorporation of strontium into dolomite and its implications for the formation of ancient dolomites. Geology 18 (5), 387–391.
Virtasalo, J.J., Endler, M., Moros, M., Jokinen, S.A., Hämäläinen, J., Kotilainen, A.T., 2016. Base of brackish-water mud as key regional stratigraphic marker of mid-Holocene marine flooding of the Baltic Sea Basin. Geo Mar. Lett. 36 (6), 445–456.
Wang, T., Simoneit, B.R.T., 1995. Tricyclic terpanes in Precambrian bituminous sandstone from the eastern Yanshan region, North China. Chem. Geol. 120 (1–2), 155–170.
Wehrli, B., Stumm, W., 1989. Vanadyl in natural waters; adsorption and hydrolysis promote oxygenation. Geochem. Cosmochim. Acta 53 (1), 69–77.
Wei, X., Zhang, T., Huang, J., Liang, X., Yao, Q., Tang, X., 2011. Sequence stratigraphy characteristics and filling evolution models of Paleogene in Baiju Sag. Subei Basin 32 (4), 427–437.
Wei, W., Algeo, T.J., 2020. Elemental proxies for paleosalinity analysis of ancient shales and mudrocks. Geochem. Cosmochim. Acta 287, 341–366.
Wei, W., Algeo, T.J., Yangbo, L., Yongchao, L., Huiming, L., Shoupeng, Z., Li, P., Jingyu, Z., Lin, C., 2018. Identifying marine incursions into the Paleogene Bohai Bay Basin lake system in northeastern China. Int. J. Coal Geol. 200, 1–17.
Westerhold, T., Röhl, U., Donner, B., McCarren, H.K., Zachos, A.J.C., 2011. A complete high-resolution Paleocene benthic stable isotope record for the central Pacific (ODP Site 1209). Paleoceanogr. Paleoclimatol. 26 (2), PA2216.
Westerhold, T., Röhl, U., Raffi, I., Fornaciari, E., Monechi, S., Reale, V., Bowles, J., Evans, H.F., 2008. Astronomical calibration of the Paleocene time. Palaeogeogr. Palaeoclimatol. Palaeoecol. 257 (4), 377–403.
Xia, L., Cao, J., Hu, S., Li, S., 2019. How marine incursion influences the quality of lacustrine source rocks; the Paleogene Nanxiang Basin, eastern China. AAPG Bull. 103 (5), 1071–1096.
Xiao, W., Cao, J., Luo, B., He, Y., Zhou, G., Zuo, Z., Xiao, D., Hu, K., 2020. Marinoan glacial aftermath in South China: paleo-environmental evolution and organic carbon accumulation in the Doushantuo shales. Chem. Geol. 555, 119838.
Xu, C., Shan, X., He, W., Zhang, K., Rexiti, Y., Su, S., Liang, C., Zou, X., 2021. The influence of paleoclimate and a marine transgression event on organic matter accumulation in lacustrine black shales from the Late Cretaceous, southern Songliao Basin, Northeast China. Int. J. Coal Geol. 246, 103842.
Xu, H., C, G.S., Hou, D., 2019. The occurrence of isorenieratane and 24-*n*-propylcholestanes in Paleogene lacustrine source rocks from the Dongying Depression, Bohai Bay Basin; implications for bacterial sulfate reduction, photic zone euxinia and seawater incursions. Org. Geochem. 127, 59–80.
Yang, Z., Tao, K., Shen, W., Wang, L., Yang, X., 1998. Geochemistry and source characters of the concealed eogene basalts in North Jiangsu basin. Acta Petrol. Sin. 14 (3), 332–342.
Zachos, J., Pagani, M., Sloan, L., Thomas, E., Billups, K., 2001. Trends, rhythms, and aberrations in global climate 65 Ma to present. Science 292 (5517), 686–693.
Zachos, J.C., Roehl, U., Schellenberg, S.A., Sluijs, A., Hodell, D.A., Kelly, D.C., Thomas, E., Nicolo, M., Raffi, I., Lourens, L.J., 2005. Rapid acidification of the ocean during the paleocene-eocene thermal maximum. Science 308 (5728), 1611–1615.
Zhang, S., Zhu, X., Zhong, D., Liang, B., Cao, B., He, X., 2004. The character of sequence framework of tertiary and upper cretaceous in gaoyou sag, Subei Basin. Acta Sedimentol. Sin. 22 (3), 393–399.
Zhao, Z., Cai, X., Qian, Z., 1993. A study of funing Formation of North Jiangsu basin. Petrol. Explor. Dev. 20 (4), 52–57.
Zheng, Y., Anderson, R.F., van Geen, A., Kuwabara, J.S., 2000. Authigenic molybdenum formation in marine sediments; a link to pore water sulfide in the Santa Barbara Basin. Geochem. Cosmochim. Acta 64 (24), 4165–4178.
Zhou, S., 1982. Discussion on crustal movements in northern Jiangsu on the basis of sporo-pollen. Oil Gas Geol. 3 (3), 277–281.
Zhou, X., Jiang, Z., Quaye, J.A., Duan, Y., Hu, C., Liu, C., Han, C., 2019. Ichnology and sedimentology of the trace fossil-bearing fluvial red beds from the lowermost member of the Paleocene Funing Formation in the jinhu depression, Subei Basin, East China. Mar. Petrol. Geol. 99, 393–415.
Zou, C., Zhu, R., Chen, Z., Ogg, J.G., Wu, S., Dong, D., Qiu, Z., Wang, Y., Wang, L., Lin, S., Cui, J., Su, L., Yang, Z., 2019. Organic-matter-rich shales of China. Earth Sci. Rev. 189, 51–78.
Zumberge, J.E., 1987. Prediction of source rock characteristics based on terpane biomarkers in crude oils: a multivariate statistical approach. Geochem. Cosmochim. Acta 51 (6), 1625–1637.